

Article

A Mechanistic Collective Cell Model for Epithelial Colony Growth and Contact Inhibition

Sebastian Aland,^{1,*} Haralambos Hatzikirou,^{1,2} John Lowengrub,^{3,*} and Axel Voigt^{1,2,4}¹Department of Mathematics and ²Center for Advancing Electronics Dresden (CfAED), Technische Universität Dresden, Dresden, Germany;³Department of Mathematics and Center for Complex Biological Systems, University of California Irvine, Irvine, California; and ⁴Center for Systems Biology Dresden (CSBD), Dresden, Germany

ABSTRACT We present a mechanistic hybrid continuum-discrete model to simulate the dynamics of epithelial cell colonies. Collective cell dynamics are modeled using continuum equations that capture plastic, viscoelastic, and elastic deformations in the clusters while providing single-cell resolution. The continuum equations can be viewed as a coarse-grained version of previously developed discrete models that treat epithelial clusters as a two-dimensional network of vertices or stochastic interacting particles and follow the framework of dynamic density functional theory appropriately modified to account for cell size and shape variability. The discrete component of the model implements cell division and thus influences cell size and shape that couple to the continuum component. The model is validated against recent *in vitro* studies of epithelial cell colonies using Madin-Darby canine kidney cells. In good agreement with experiments, we find that mechanical interactions and constraints on the local expansion of cell size cause inhibition of cell motion and reductive cell division. This leads to successively smaller cells and a transition from exponential to quadratic growth of the colony that is associated with a constant-thickness rim of growing cells at the cluster edge, as well as the emergence of short-range ordering and solid-like behavior. A detailed analysis of the model reveals a scale invariance of the growth and provides insight into the generation of stresses and their influence on the dynamics of the colonies. Compared to previous models, our approach has several advantages: it is independent of dimension, it can be parameterized using classical elastic properties (Poisson's ratio and Young's modulus), and it can easily be extended to incorporate multiple cell types and general substrate geometries.

INTRODUCTION

The regulation of cell division, cell size, and cell arrangement is central to tissue morphogenesis. A detailed understanding of this regulation provides insight not only into the development and regeneration of normal tissues but also into carcinogenesis when regulation breaks down. Although regulation of cell division and growth has been traditionally studied via signaling pathways triggered by diffusible chemical species, the importance of mechanical constraints and mechanotransduction is increasingly recognized (see, e.g., the review (1) focusing on mechanical forces in epithelial tissue, which provides an important model system for the study of regulation of cell division, growth, and arrangements).

The dynamics of growing epithelial tissues is characterized by a delicate interplay of cell-cell interactions and macroscopic collective motion. In cultures of normal epithelial cells, as the density of cells increases due to proliferation and cell growth, the cells lose their ability to move freely. Mitotic arrest occurs and the cells acquire an epithelial morphology. This process is known as contact inhibition. In Puliafito et al. (2), detailed *in vitro* studies of epithelial

tissue dynamics using Madin-Darby canine kidney (MDCK) cells were performed, and a quantitative analysis of the evolution of cell density, cell motility, and cell division rate was presented. It was shown that inhibition of mitosis is a consequence of mechanical constraints that result in reductive cell division, which leads to an overall decrease in cell size, rather than just being a consequence of cell contact. Cell growth, division, migration, and contact inhibition have also been seen to play a role in glass-like transitions from liquid-like to solid-like behavior in clusters of MDCK cells (3).

Previously, mechanically based models were used to simulate the dynamics of a collection of epithelial cells in a variety of contexts. For example, a fully continuous description considering the epithelium as an elastic medium was considered in Shraiman (4), where the effect of mechanical stress on cell proliferation was investigated. Although contact inhibition could be described qualitatively, this formulation prevents quantification at the level of a single cell. Cell-level resolution is achieved in discrete descriptions such as the Cellular Potts model (see, e.g., Scianna and Preziosi (5)) and vertex models (see, e.g., Farhadifar et al. (6)). In the former, cells are modeled as a collection of grid points on a Cartesian mesh. The system is equipped with an energy that accounts for biophysical properties including adhesion, cell stiffness, and motility,

Submitted February 2, 2015, and accepted for publication August 3, 2015.

*Correspondence: sebastian.aland@tu-dresden.de or lowengrub@math.uci.edu

Editor: Ruth Baker.

© 2015 by the Biophysical Society
0006-3495/15/10/1347/11



<http://dx.doi.org/10.1016/j.bpj.2015.08.003>

and the dynamics occur stochastically using a Boltzmann acceptance function that determines whether two grid points should exchange their properties. In the vertex model, epithelial cells are described by a two-dimensional network of vertices, representing the cell edges (see Fig. 1, A and B). Stable network configurations are achieved by a mechanical force balance between an outward force due to limited cell compressibility and an opposing line tension resulting from the combined effect of myosin-dependent cortical contractility and cell-cell adhesion. These forces are incorporated into an energy function that is calculated and used to update the position of each vertex over time. Within this framework, the contributions of cell growth, mitosis, and cell intercalation are incorporated to predict the evolution of tissue toward a stable mechanical equilibrium. Vertex models have been successfully used to model processes such as the shaping of compartment boundaries in the developing *Drosophila* wing (7) and morphogen distribution and growth control (8), among other processes. It should be noted that in vertex models, other mechanical contributions, such as cell-matrix adhesion (9), centripetal cytoplasmic contractile activity (10), or the ability of cells to change neighbors, which can be described as tissue fluidity, are either missing or have only been incorporated in an ad hoc fashion. More recently, vertex models have been extended to three space dimensions (11–13).

Collective cell motion in epithelial sheets has also been quantitatively described by stochastic particle models (see, e.g., Sepulveda et al. (14)). In this approach, each cell is reduced to its center point (although in a few studies, cell size (see, e.g., Macklin et al. (15)) and shape (see, e.g., Schaller et al. (16)) have been taken into account in the context of cancer) and the dynamics are described by Langevin-like systems of equations. The stochastic motion of a cell is modeled by an Ornstein-Uhlenbeck process. Dissipation due to adhesion and friction is taken into account through a linear damping term. The interaction with neighboring cells is modeled by an intercell potential that is repulsive at short ranges and attractive at longer distances. Such models have been able to quantitatively reproduce statistical characteristics of the cell velocity field and positions at early times in controlled wound healing experiments on MDCK cells (14). However, although cell intercalation was natu-

rally included, cell growth and mitosis either were not considered or were only accounted for in an implicit manner by a density-dependent noise term.

It is worthwhile to relate stochastic particle models with vertex models, although it is difficult to directly compare the two. A qualitative comparison between these models can be made by constructing a Voronoi diagram for the center points in the particle model, which can then be used to relate epithelial cell packings in the particle and vertex models to one another (see Fig. 1 C). Our goal here is not to make the link between the two approaches quantitative, but rather to use the stochastic particle model as a starting point to derive a coarse-grained continuum model, following the framework of dynamic density functional theory (DDFT). By extending this framework to account for cell size and shape variability, we obtain a continuum partial differential equation (PDE) for the epithelial cell density that provides single-cell resolution and yet can describe elastic, plastic, and viscoelastic deformations at larger scales. Such a modeling approach was previously sketched in Chauviere et al. (17) for solid tumor growth, but no simulation results were provided. This approach is motivated by the successes of DDFT in simulating inhomogeneous, non-equilibrium interacting particle systems with Brownian dynamics (18). Because of the continuum formulation, the model extends straightforwardly to three dimensions. The model can easily incorporate other biophysical phenomena, such as flow, nutrient diffusion, and active motion via chemotaxis. Unlike the approach described in Chauviere et al. (17), cell division is accomplished using a discrete approach, making the overall system a hybrid continuum-discrete model. We will demonstrate the quantitative predictive power of such a modeling approach by comparing our simulation results with the detailed analysis of contact inhibition in Puliafito et al. (2).

MATERIALS AND METHODS

In the DDFT framework, a discrete particle system is modeled via a continuum-level continuity equation for a noise-averaged density field, $\rho(x, t) = \langle \sum_i \delta(x_i(t) - x) \rangle$, where the angled brackets denote averaging and $x_i(t)$ denotes the particle positions. A key idea is that the averaged density evolves on experimentally relevant long timescales (seconds to

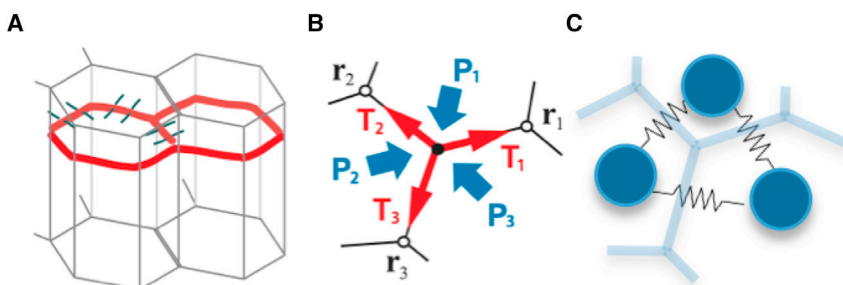


FIGURE 1 (A) A sketch of epithelial cells, for which we assume that the mechanical interactions act in the plane of the adherens junctions. (B) Two-dimensional vertex representation of epithelial cells with balancing forces on a vertex due to line tension (red) and pressure (blue). (C) Two-dimensional particle representation of epithelial cells, with balancing forces represented by springs, and a corresponding Voronoi diagram. To see this figure in color, go online.

hours for representative experimental growth conditions) while still allowing the individual locations of the particles (peaks of the density field) to be determined. The continuity equation accounts for correlations among the particles through a nonlocal contribution involving the direct two-point correlation function (18) and derives from a gradient flow of a nonlocal free-energy function. Expanding the free-energy function to lowest order, the nonlocal equation can be reduced to a high-order PDE, known as the phase field crystal (PFC) model (19,20). The PFC was introduced as a model for elasticity in crystalline structures (21) and is popular in condensed-matter physics because of its simplicity and its ability to combine particle-particle interactions with macroscopic material behavior. Here, we adapt the PFC model to account for cell size and shape variability.

Conserved gradient flow for cell density

Like the DDFT system, the PFC model possesses a free energy that involves the averaged density, ρ , as well as parameters that describe the equilibrium epithelial cell packing. The density evolves according to a generalized continuity equation that arises from a conserved gradient flow model. The free-energy expression is based on (22)

$$E = \int_{\Omega} \frac{1}{4}\tilde{\rho}^4 + \frac{1+r}{2}\tilde{\rho}^2 - cq|\nabla\tilde{\rho}|^2 + \frac{c^2}{2}[\nabla \times (q\nabla\tilde{\rho})]^2 dx, \quad (1)$$

where $\tilde{\rho} = \rho - \bar{\rho}$ denotes the difference between the epithelial cell density and a reference value, $\bar{\rho}$. In the remainder of this article, we omit the tilde and simply use ρ to denote the density difference. The parameter q can be interpreted as the equilibrium epithelial cell area, which we will spatially vary, as described below, to account for different cell sizes. The constant $c = \sqrt{3}/8\pi^2$ is introduced to scale q such that it can be interpreted as the cell area, at least in hexagonal ordering of cells, as given by the one-mode approximation (see the [Supporting Material](#) for details). The first two terms in Eq. 1 define a double well potential for appropriate values of $r < 0$, with two minima corresponding to the presence of a cell or no cell. The third term, a gradient term, can also be found in classical Ginzburg-Landau type models, although the sign here is negative. Hence, the term favors rapid changes in the density. Conversely, the fourth term, which is a higher-order term, gives a positive contribution penalizing density changes. The interplay of these two terms favoring and penalizing density changes results in a preferred length scale of spatial density oscillations.

A simple illustration may be helpful to understand the connection between the cells, the density field, and elastic interactions. Let us consider a one-dimensional example for constant q . In this case, the energy in Eq. 1 is minimized by periodic functions. If we consider density to contain only one mode (the so-called one-mode approximation), these functions must take the form $\rho(x) = A\cos(2\pi x/a_{eq}) + \rho_0$ for constants A and a_{eq} . We interpret the peaks of this function as the (center) positions of cells, with the lattice spacing given by a_{eq} . Now, let's plug the above density into energy (Eq. 1) for variable lattice spacing, a . We obtain the second-order expansion, $E(a) = E(a_{eq}) + (1/2)2A^2(a - a_{eq})^2$, which is basically Hooke's law, since any change in the lattice spacing increases the energy quadratically. The parameters A and a_{eq} are determined by energy minimization within this class of functions (see the [Supporting Material](#) for details). In this way, the model naturally captures linear elasticity of cells on a microscopic scale, resulting in repulsion as soon as cells get too close to each other and attraction (adhesion), which prevents cells from going adrift. The parameter $r < 0$ together with the average cell density, ρ_0 , are used to fit the first peak in the two-point direct correlation function of the underlying intercell potential and are related to elastic parameters (e.g., Poisson's ratio and Young's modulus) of the epithelial cell cluster (20,23). For example, from the above energy expansion, we can directly conclude that the Young's modulus in this case is $2A^2$ (see the [Supporting Material](#) for details). For a

further overview of the PFC model and a summary of the underlying concepts, we refer to the book by Elder and Provatas (24) and a recent review article (25).

All movement of cells in our model is driven by the minimization of the energy in Eq. 1. To realize this minimization, we consider a conserved gradient flow, as in Elder and Grant (22):

$$\partial_t \rho = \eta \Delta \frac{\delta E}{\delta \rho}, \quad (2)$$

where η is a mobility parameter, which can be interpreted as modeling the combined effects of cell-substrate adhesion and friction between the cells and a surrounding viscous fluid. The variational derivative, $\delta E/\delta \rho$, is given by

$$\frac{\delta E}{\delta \rho} = \rho^3 + (1+r)\rho + 2c\nabla \times (q\nabla\rho) + c^2\nabla \times (q\nabla(\nabla \times (q\nabla\rho))).$$

We can interpret the (local) maxima in the density field as the centers of the epithelial cells. Within this approach, ρ is globally conserved. However, the number of maxima, and thus the number of cells, is not. If a cell disappears, it diffuses into the surrounding cells, leading to a decrease in the maxima and finally to their disappearance. To overcome this problem, we extend the continuous PFC model by a semidiscrete term taking into account the discrete position of each cell.

Let the cells be numbered by $i = 1, \dots, N$, where $N = N(t)$ is the total number of cells that may change over time. For cell i , we denote the corresponding local maximum of the density field by ρ_i and the position of this maximum by x_i , hence $\rho(x_i) = \rho_i$. From the positions of the local maxima, we may compute the Voronoi cells, Ω_i , which serve to represent the geometry of epithelial cell i . Correspondingly, we introduce the characteristic function of each cell, χ_i , defined by $\chi_i = 1$ in Ω_i and 0 otherwise. The region without cells is denoted by $\chi_0 = 1 - \sum_{i=1}^N \chi_i$. In equilibrium, Ω_i and χ_i are related to the equilibrium cell area, q , which was assumed to be constant in the original model (21). Here, however, we allow q to be space-dependent to account for cell-size variability that can occur during the evolution due to cell division. That is, $q = \sum_{i=0}^N q_i \chi_i$, where q_i is a measure of the epithelial cell area of cell i , which can be time-dependent. (See the discussion in the next section.) Note that the space-dependent q defined above gives for any point in space the equilibrium area of the cell that is present at that point. In the region without cells ($\chi_0 \approx 1$), we set $q_0 = 1/c$.

To ensure that the number of cells is conserved between mitotic or apoptotic events, we need local mass conservation for each cell. To achieve this, the evolution equation (Eq. 2) is modified to

$$\partial_t \rho = \eta \Delta \frac{\delta E}{\delta \rho} + \alpha \sum_{i=1}^N (\rho_{\max} - \rho_i) \max(\rho, 0) \chi_i + \beta (\rho_{\min} - \rho) \chi_0, \quad (3)$$

where α and β are relaxation constants and ρ_{\max} and ρ_{\min} are the approximate equilibrium values of the cell density, ρ , in the peak regions and in the region without cells, respectively. We provide a detailed motivation for Eq. 3 in the [Supporting Material](#), including the calculation of ρ_{\max} and ρ_{\min} a priori from a one-mode approximation.

Cell growth and mitosis

We now incorporate cell growth and mitosis. The equilibrium area of each cell may change over time, as cells may increase their area until they divide. After division, of course, the equilibrium cell area is reduced abruptly. Before division, we assume that there is a cell-dependent rate, k_i , such that

$$\partial_t q_i = k_i. \quad (4)$$

In this work, we take k_i to be constant for each cell. More generally, k_i may depend on the concentration of available nutrients or growth factors. Here, we concentrate on modeling contact inhibition and therefore take into account that in densely packed regions, a cell might not have enough space to grow. Comparing the actual cell area, $|\Omega_i| = \int \chi_i dx$, with the target equilibrium cell area, q_i , we obtain an approximation for the cell compression (26). If the ratio $\int \chi_i dx / q_i$ is below a threshold value, the growth of a cell is prohibited by prescribing $\partial_t q_i = 0$. Here, we take 0.9 as the threshold.

Mitosis can be initiated by different events. In the simulations here, we use the cell lifetime as a trigger, as suggested by the experiments in Puliafito et al. (2). In particular, mitosis is initiated when the cell reaches a prescribed lifetime, $t_i \geq t_{div,i}$, which is taken to be random (see [Simulation setup](#)). To perform division, we replace the local maximum at x_i with two new maxima using Gaussians in the neighborhood of the original maximum. The position of the new maxima can be chosen in different ways and may affect the cell topology (27). Here, we are free to choose any cleavage-plane mechanism, but we restrict our numerical tests to three different cleavage mechanisms (see [Simulation setup](#) and [Fig. 5](#)). In each case the daughter cells are put at a distance of $(1/2\sqrt{\pi})\sqrt{q_i}$ on opposite sites from the original mother cell and the cell area of the two daughter cells is set such that $q_{child} = q_i/4$. This choice is motivated by the experimentally observed drop in cell area at mitotic events (2) (see [Fig. 4 A](#)). In particular, the cell areas in the experiments are found to decrease at every mitotic event by a factor of ~ 4 . As we see below, the model predicts that the daughter cells grow quickly into the space that was previously occupied by the mother cell, consistent with the experiments. Apoptosis is not considered in the simulations presented here but can be included easily by removing a cell according to a given criteria like cell age, available nutrients, number of divisions, or random selection.

RESULTS

The complete algorithm of our PFC model for epithelial cells is summarized for one time step in [Fig. 2](#). More de-

tails on the numerical implementation can be found in the [Supporting Material](#). For all simulations, we use the nondimensional PFC equations given in Eq. 3 using the characteristic length- and timescales $L = 0.59 \mu\text{m}$ and $T = 50 \text{ s}$. Accordingly, T determines the time step for the numerical scheme and L is small enough to ensure that there are 100 grid points in cells as small as $35 \mu\text{m}^2$. The typical computational time for the simulations presented in the following is one week. This time is mostly due to the simple explicit calculation of the nearest-neighbor cell for the Voronoi tessellation in every time step. A more sophisticated algorithm, e.g., using k -d trees (28), is expected to reduce the computational time by at least one order of magnitude.

Simulation setup

We start with a small colony of nine epithelial cells with areas q_i randomly chosen in the interval $[500 \mu\text{m}^2, 2000 \mu\text{m}^2]$ and placed in the center of the computational domain. The division time, $t_{div,i}$, after which cell i divides depends on q_i and is motivated by the Hill function given in Puliafito et al. (2). The explicit form reads $t_{div,i} = 0.74d(q_i^4 + (170\mu\text{m}^2)^4)/q_i^4 + \mathcal{P}([0, 0.02d])$, where $\mathcal{P}(X)$ denotes a random variable uniformly distributed in X and d denotes days. The average cell division time is $0.75d$ for larger cells ($q_i > 170 \mu\text{m}^2$), whereas the division time tends to infinity for smaller cells ($q_i \ll 170 \mu\text{m}^2$). The cell growth rate is set to $k_i > 2000 \mu\text{m}^2/d$, which implies that the epithelial cells on average reach the area of their mother cell during the cell-cycle time if they can freely grow. The remaining parameters are in nondimensional form: $\alpha = 1, \beta = 1$, and we vary η from 5 to 20.

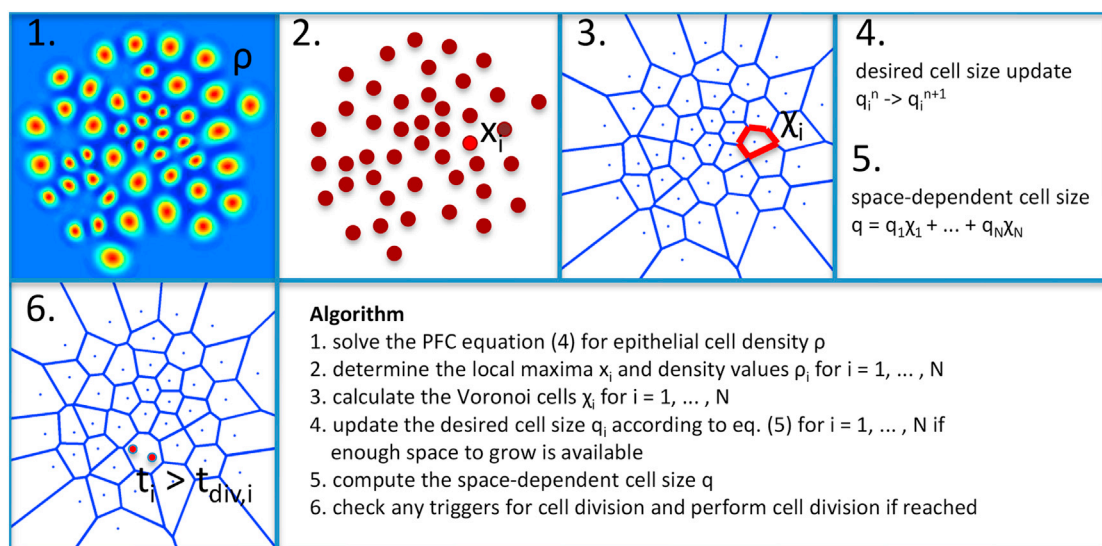


FIGURE 2 Schematic description of the numerical algorithm. The artifacts of the Voronoi cells at the periphery are only graphical and do not influence the computation. To see this figure in color, go online.

Growth experiments

Fig. 3 shows snapshots of the density field, ρ , describing the epithelial cell positions at various times and the corresponding Voronoi diagrams that characterize the cell packings. The colony expands over time, which is enabled by repulsive forces between the epithelial cells, where cells push their neighbors away as they grow. A cluster of 1369 cells has developed by the final time, with smaller cells in the inner region and larger cells in the outer region.

An analysis of the numerical results is shown in **Fig. 4**, together with comparisons with experimental results from Puliafito et al. (2). In **Fig. 4 A**, the evolution of the colony areas is shown for the simulation results with different mobilities, η , and the experimental results (*circles*). The experimental and simulation results are scaled as described below and are in excellent agreement. Reference results are shown for exponential growth (*black line*) and quadratic growth (*gray line*). The results show that there is a transition at about $2d$ from exponential growth to quadratic growth. This can be explained as follows, using arguments from ordinary differential equation models of population growth. At early times, since all cells may grow and divide, the cluster area, A , grows exponentially: $dA/dt \sim \lambda A$, where $\lambda^{-1} \sim 0.75d$, the average epithelial cell-cycle time. As the cluster grows, mechanical constraints (contact inhibition) due to reduced cell movement and lack of space prevent the interior cells from growing in size, although interior cells continue to divide by reductive cell division until their area drops below the critical threshold. This leads to larger numbers of smaller cells, with the total areas being approximately conserved. In the simulations, we find that the growth in size in the colony is due to a ring of growing

and proliferating cells at the colony edge. Assuming that cells only proliferate in this rim, with the same cell-cycle time as before, leads to a colony growth law, $dA/dt \sim 2\sqrt{\pi}\lambda r_{\text{rim}}\sqrt{A}$, where r_{rim} is the thickness of the proliferating rim (here assumed to be constant). Thus, at late times, $A \sim \pi\lambda^2 r_{\text{rim}}^2 t^2$. Hence, a constant-thickness growing rim of cells corresponds to the quadratic growth, which was found in the simulations. The encountered exponential-to-algebraic crossover in colony growth observed here has also been found in other models and experiments for cancer growth (29). There, the crossover is not caused by contact inhibition but rather is attributed to limited resources and the ability of cancer cells to enter quiescence upon starvation.

The above analysis of colony growth also reveals a scaling invariance: if $A(t)$ is a solution of the growth law, then $\bar{A}(\bar{t}) = A(t + t_{\text{shift}})/A_{\text{ref}}$ is also a solution of the growth law, with corresponding rim thickness $\bar{r}_{\text{rim}} = r_{\text{rim}}/\sqrt{A_{\text{ref}}}$. Thereby, $t_{\text{shift}} = -\lambda^{-1}\ln(A_{\text{ref}})$, since the time span of exponential growth increases by t_{shift} . Hence, there is effectively only one free variable (A_{ref} or t_{shift}) to fit. We take advantage of this scale invariance to compare the simulated and experimental results. In **Fig. 4 A**, the scaled results, $\bar{A}(\bar{t})$, are plotted as a function of \bar{t} for the different cases where A_{ref} is chosen empirically to match the $\eta = 10$ simulations. For example, in the experiments, the colony area is ~ 30 times larger than the one obtained for the $\eta = 10$ simulation. By considering $A_{\text{ref}} = 30$, we calculate $t_{\text{shift}} = 4.5d$. We find $\bar{r}_{\text{rim}} \approx 70\mu\text{m}$, which corresponds to a proliferating rim thickness in the experiments of $r_{\text{rim}} \approx 385\mu\text{m}$. Similar scalings are used for the numerical results. In particular, increasing the mobility, η , leads to larger cluster sizes, delays the

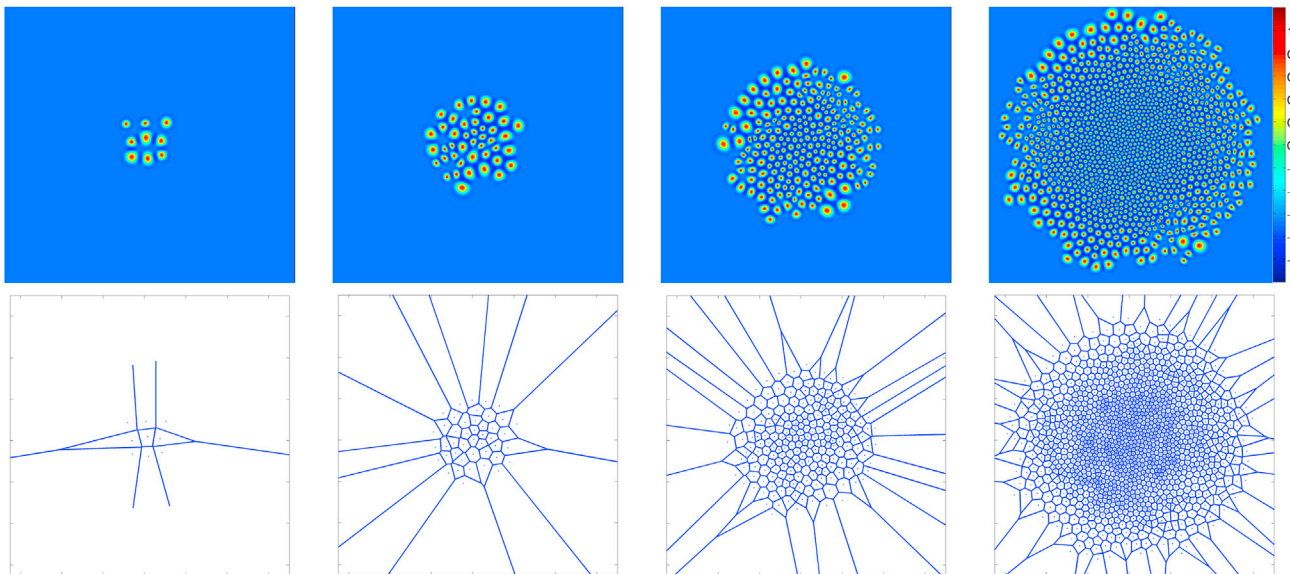


FIGURE 3 Epithelial cell density field, ρ , at times $t = 0.05$ days, 1.73 days, 3.46 days, and 5.77 days (*left to right*), with corresponding Voronoi diagrams (*lower row*). The artifacts of the Voronoi cells at the periphery are only graphical and do not influence the computation. To see this figure in color, go online.

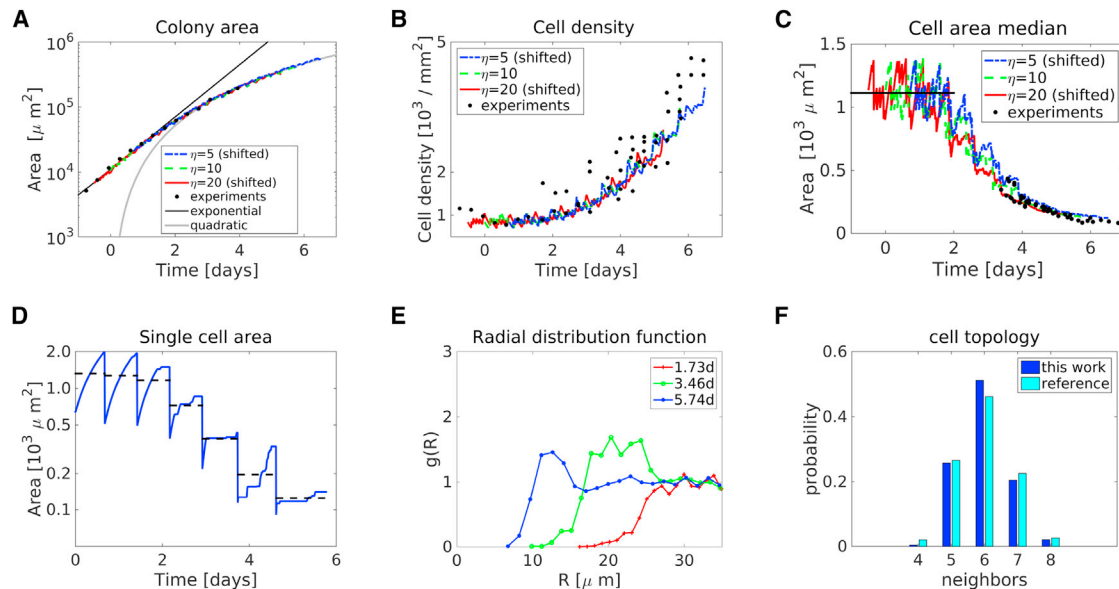


FIGURE 4 Analysis of cell areas and arrangements. (A) Total area of the spreading colony. The black line corresponds to exponential growth with the average epithelial cell cycle time 0.75 days. The gray line corresponds to quadratic growth, and the symbols correspond to scaled results from the experiments in Puliafito et al. (2) (see text for additional description). The blue dot-dashed, green dashed, and red lines correspond to scaled simulation results for different mobilities, η , as labeled. (B) The corresponding average cell densities remain almost constant until $\bar{t} \approx 2$ days and they grow rapidly thereafter. The plot is superimposed on the results from Fig. 1 C of Puliafito et al. (2) with shifted time (see text). (C) The median of the area distribution of epithelial cells in the center region ($< 100 \mu\text{m}$ distance to the center) is nearly constant (solid black line) during exponential growth and shows a rapid decrease when contact inhibition sets in at $\bar{t} \approx 2$ days. (D) Area of a single epithelial cell as a function of time remains constant before $\bar{t} \approx 2$ days and subsequently decreases. The dashed black lines are average epithelial cell areas between mitosis events. Results correspond to $\eta = 10$. (E) Radial distribution function of simulated cell distributions with $\eta = 10$ at different times, as labeled. The appearance of a peak and trough in the quadratic growth regime indicates short-range ordering of cells. (F) Histogram of the distribution of the cellular coordination number (number of direct cell neighbors) at $\eta = 10$. The reference distribution is from Puliafito et al. (2). To see this figure in color, go online.

transition from exponential to quadratic growth by making the cells more mobile, and thus extends the regime of free growth (see the [Supporting Material](#)). As also shown in the [Supporting Material](#), increasing the Young's modulus has a similar effect.

During the exponential phase of growth, the cell density (Fig. 4 B), average cell area (Fig. 4 C), and individual cell area (Fig. 4 D) remain nearly constant. That is, daughter cells have approximately the same areas as mother cells. After $\bar{t} \approx 2d$, growth is inhibited and expansion of the colony periphery cannot keep up with cell proliferation in the bulk. Hence, the density of bulk cells increases due to the limited space, and the cell areas decrease due to reductive cell division. Hence, daughter cells can only grow until they reach approximately one-half of the area of the mother cells, in agreement with the experimental measurements (see Figs. 3 C and 4 A in Puliafito et al. (2)).

Cell arrangements

To quantify the cell arrangements, we plot the radial distribution function in Fig. 4 E. The radial distribution function, $g(R)$, measures the probability of finding a cell at distance R from a given reference cell. It is determined by measuring the distances between all cell pairs and binning them into

a histogram. The histogram ordinate is divided by R and normalized such that far-away cells have $g(R) = 1$. Hence, a value of 1 indicates no correlation between the cell distances (gas-like behavior). This behavior is found in the exponential growth regime. The emergence of a peak (and a trough behind) in the quadratic growth regime indicates the development of short-range ordering of cells. This indicates the emergence of amorphous solid behavior, which is in agreement with previously found glass-like properties of growing cell clusters (3). A similar transition is observed in experiments (see Fig. 3 D of Puliafito et al. (2)).

The number of cell neighbors, also referred to as polygon class or cellular coordination number, gives another measure for the homogeneity of epithelial packings and has been investigated in various theoretical and experimental studies (see, e.g., other studies in the literature (6,27,30–33)) of different biological systems. In general, it is found that many tissues organize such that 45% of cells have six neighbors, whereas 25% and 20% have five and seven neighbors, respectively (34). Similar results are obtained in our simulations (see Fig. 4 F), with 51%, 26%, and 20% of six-sided, five-sided, and seven-sided cells, respectively, again in good agreement with Puliafito et al. (2). The coordination number is measured at the final time, omitting the cells at the boundary of the colony. The standard PFC model tends to organize

cells homogeneously in a hexagonal packing. This can be altered by constraints, e.g., due to an underlying curvature (35–37) or, as in the case presented here, an inhomogeneous distribution of cell sizes and the presence of mitosis. The good agreement between the simulations and experiments (2) was achieved without any parameter adjustments.

Next, we investigate the influence of the cleavage plane, e.g., the perpendicular bisector between the two progeny at mitosis. The cleavage plane is known to have a significant influence on the arrangement of epithelial cells in models (see, e.g., Patel et al. (27)), and in experiments (see, e.g., Gibson et al. (34)). Empirical investigations show that many monolayer cell sheets across the plant and animal kingdoms converge on a default equilibrium distribution of cellular shapes, with ~45% hexagons, 25% pentagons, and 20% heptagons (34). Using numerical simulations (27), we found that the cell topology is highly sensitive on the cleavage plane. In particular, the number of six-sided cells decreases for cleavage-plane mechanisms from cutting the longest edge (corresponding to the best angle) to cutting the shortest edge (corresponding to the worst angle). We confirm this observation here using three different cleavage planes, which are depicted in Fig. 5. The two daughter cells may be put in a position such that they have the most (*best angle*) or least space (*worst angle*), or they could be randomly aligned (*random angle*). The resulting cell coordination numbers are plotted in Fig. 6 for the various cleavage-plane mechanisms (experimental data are from Fig. S1 B in Puliafito et al. (2)). Here, we used $\eta = 10$, since our simulations revealed that the mobility, η , has no noticeable influence on the coordination number (results not shown).

As pointed out above, the best-angle mechanism produces a cell arrangement that is too regular (e.g., too many cells with six neighbors). Making the cleavage plane random leads to a more heterogeneous cell arrangement and produces a number of cell neighbors very close to the general reference values from Fig. S1 B of Puliafito et al. (2). Heterogeneity is further increased by using the worst-angle mechanism. However, the resulting number of six-sided cells is much lower than that reported in experiments. Our results are also in qualitative agreement with the simulation results of Patel et al. (27). However, since their simulation does not take into account cell rearrangements, they

might overestimate the effect of the cleavage plane, which is confirmed if we compare their absolute numbers with ours. Our results suggest that MDCK cells may indeed choose the cleavage plane in a random manner (determined by intracellular processes), since under these conditions our simulations demonstrate the closest agreement with experiments. It is known, however, that Voronoi tessellations, such as those used in our postprocessing, may lead to a cell packing that is too homogeneous. This could influence our conclusions, since the best-angle and random-angle results are fairly close to one another. We note that Gibson et al. (34) present evidence that the best-angle division is most consistent with neighbor-number distributions of epithelial cells in the *Drosophila* wing disc. Future studies will be performed to analyze cleavage-plane effects in more detail. We note that the cleavage plane has only a small influence on the total number of cells and no noticeable influence on colony area, epithelial cell density, or epithelial cell areas (results not shown).

Cell motility and elastic properties

To obtain a more complete picture of the cell movements, we plot the cell velocity averaged over the last 5 h of the simulation. Fig. 7 shows that cells in general move the fastest along the colony periphery, whereas the interior cells move slowly. These outer cells migrate mostly away from the center, as expected. The inner cells move much more slowly and their movement is less oriented and more chaotic, indicating that interior motion is due primarily to cell rearrangements in the colony interior. Thus, interior cells may move past each other slowly to rearrange, a feature that is problematic to resolve with standard vertex models. The results are in general agreement with the experiments of Puliafito et al. (2), although the cell velocities found in the simulation are ~10 times smaller than those found in the experiments. This is consistent with the difference in the simulated and experimental cluster sizes and indicates that the mobility used in the simulations ($\eta = 10$) overpredicts the effects of cell-substrate adhesion (and drag).

The mechanical stress acting on the cells has been proposed by Puliafito et al. (2) as an important step toward understanding the contact inhibition phenomenon. Here, we

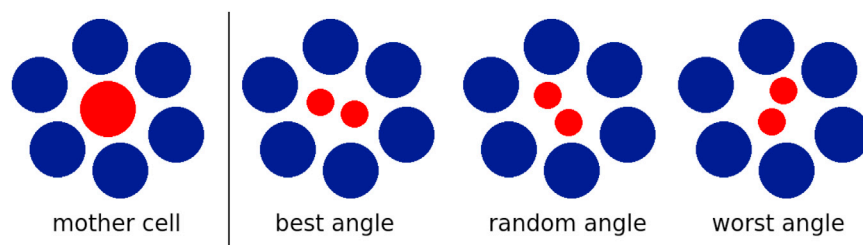


FIGURE 5 Schematic of different cleavage-plane mechanisms. A dividing mother cell (*large red circle*) may align the daughters (*small red circles*) such that they have the most (*best angle*) or least space (*worst angle*), or are randomly aligned (*random angle*). The blue circles denote previously existing cells. To see this figure in color, go online.

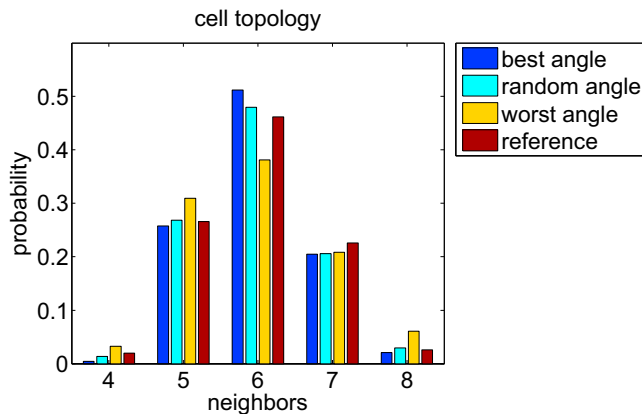


FIGURE 6 Histogram of the distribution of the cellular coordination number (number of direct cell neighbors) for different cleavage-plane mechanisms using the mobility $\eta = 10$. The random cleavage plane produces results closest to the reference (Fig. S1 B of Puliafito et al. (2)). To see this figure in color, go online.

investigate the cell bulk stress, e.g., the compression of each cell. From the target cell area, q_i , and the actual cell area, $\int \chi_i dx$, we calculate the relative compression as $1 - \int \chi_i dx / q_i$. The results are shown averaged over time according to number of neighbors and distance to the center (Fig. 8), as well as for individual cells (Fig. 9). We find that the compression is positive for all cells and increases over time (Fig. 8, left). Cells never occupy more space than they desire, which means they are not significantly pulled by adhesion with neighboring cells during the simulation. In the inner region, the average compression is $\sim 12.5\%$ (Fig. 8, right), whereas it decays to zero across the colony periphery. The maximum compression we find is $\sim 25\%$, even though cells stop growing in the simulation once they are compressed by $>10\%$. Hence, cells that are compressed $>10\%$ must have undergone a decrease in their area due to pressure from neighboring cells, rather than being compressed as a consequence of their own growth.

Another interesting observation is that cells with fewer neighbors are more compressed (Fig. 8, middle). This is

consistent with reports for particle arrangements on curved surfaces, e.g., the morphology of viral capsids where the higher bulk stress in five-sided subunits leads to buckling (see Aland et al. (38) for a detailed analysis). This result is also in agreement with Lewis's law (39), which claims that cell areas are proportional to $(n - 2)$, where n is the number of neighbors. Hence, if cell rearrangement decreases the number of neighbors of a certain cell, the area of this cell is decreased also, leading to more compression.

DISCUSSION

We have presented a mechanistic model to simulate the dynamics of epithelial cell colonies. The model, which contains both continuum and discrete features, can be derived from stochastic particle models according to the framework of DDFT appropriately modified to account for cell size and shape variability and localizing approximations. Cell-cell interactions are modeled using continuum PDEs, and cell growth and mitosis are incorporated on a discrete level. We used this model to simulate the dynamics of clusters of epithelial cells to quantify contact inhibition dynamics at the tissue and single-cell levels. The model can be easily extended to incorporate multiple cell types, and since it is a PDE-based model, it is easy to couple the model to additional PDEs so that it can be used to simulate the dependence of cell behavior on oxygen, nutrients, and growth factors.

To validate the appropriateness of the model, we compared the simulated results with detailed in vitro studies of epithelial tissue dynamics of MDCK cells in Puliafito et al. (2). We found that the model correctly predicts a transition in the growth of the colony sizes from exponential at early times to quadratic at later times. The transition occurs because of reduced cell movement and the lack of space that prevents cells in the cluster interior from growing in size (although they may still undergo reductive cell division), whereas cells in the cluster exterior move and grow more freely, providing the source of cluster-size increases at later

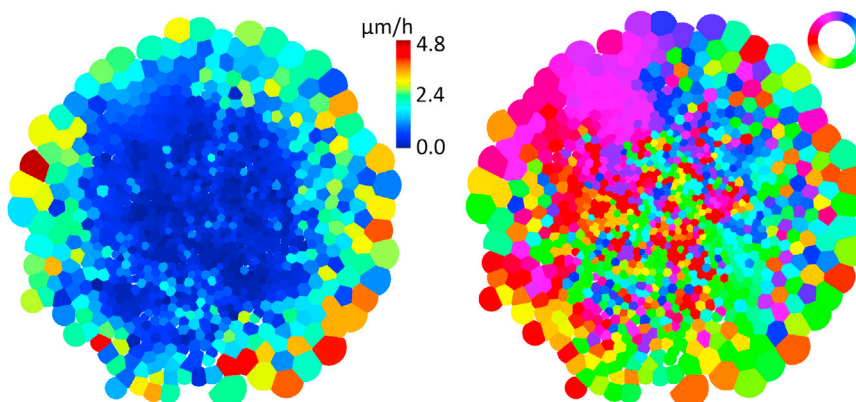


FIGURE 7 Cell velocity averaged over the last 5 h of the simulation. (Left) The velocity magnitude shows that cells in general move the fastest along the colony periphery, whereas cells in the inner region move significantly more slowly. (Right) The velocity direction is color-coded by a circular color bar and indicates that cells in the periphery move away from the center, whereas inner cells have no preferred direction of movement. To see this figure in color, go online.



FIGURE 8 Cell compression as a function of time (*left*), number of cell neighbors (*middle*), and distance to the colony center (*right*). Results indicate that the average cell compression increases with time, that cells with fewer neighbors are more compressed than cells with larger numbers of neighbors, and that cell compression is relatively constant in the inner part of the colony and decays rapidly across the outer part of the colony.

times. The transition is also associated with the emergence of short-range ordering and solid-like behavior of the cluster, which was quantified using the radial distribution function, and a constant-thickness growing (and dividing) rim of cells at the cluster edge. In the simulations, the mobility, which reflects the combined effects of cell-substrate adhesion and drag, and the Young's modulus are the primary influences on the transition from exponential to quadratic growth, with increased mobility (or Young's modulus) being associated with delayed onset of the transition because the cells are more mobile (or stiff), resulting in an extension of the free-growth regime. For the range of mobilities used, the model underpredicts the cluster sizes where the transition occurs. Computational costs prevented us from using significantly larger values of these parameters. However, an analysis of the results reveals a scale invariance such that the appropriately scaled simulation and experimental results are in excellent agreement. Excellent agreement is also obtained for the evolution of cell densities and cell areas. We

further investigated the distributions of the cellular coordination numbers (number of cell neighbors), the average cell velocity, and the mechanical bulk stress. We found that the cleavage plane is the dominant mechanism in control of cell topology but has little effect on colony morphology or growth. The experiments are most consistent with randomly chosen cleavage planes. The local cell compression is found to depend on the cell coordination numbers, with fewer neighbors resulting in larger compression, consistent with Lewis's law (39). In addition, cells in the cluster interior are found to be much more compressed and to move much more slowly and in more random directions than their exterior counterparts. Taken together, our results confirm the findings of Puliafito et al. (2), in which contact inhibition was identified as a consequence of mechanical constraints that cause successive cell divisions to reduce the cell area and not just a result of cell contact.

The model offers several methodological advantages compared to previous models. 1) The model can capture elastic, viscoelastic, and plastic deformations within a continuum framework. In particular, tissue fluidity is intrinsically included by minimization of the free energy; for example, if two cells in our model are sufficiently far from one another, the interaction forces (repulsive and attractive) vanish. The behavior of the cells in this case is independent of whether these cells are direct neighbors in a Voronoi diagram. 2) The model is dimension-independent and could therefore also be used without modification to simulate three-dimensional clusters of cells. 3) Using surface finite elements, or the diffuse domain approach, the model can be straightforwardly used on any arbitrarily curved and even time-evolving surface (see, e.g., Aland and colleagues (38,40)). For example, the model can be used for epithelial cells in the gut that move on curved crypts and villi with dynamic shapes. 4) The PDE-based approach makes it possible to use the highly developed analytical theory for stability, convergence, and error estimation of the numerical algorithm. 5) The model can be parameterized using classical elastic properties (e.g., Poisson's ratio and Young's modulus).

Although the elastic properties of cell colonies are in principle measurable, these elastic parameters are not well-known. In contrast, the mechanical properties of

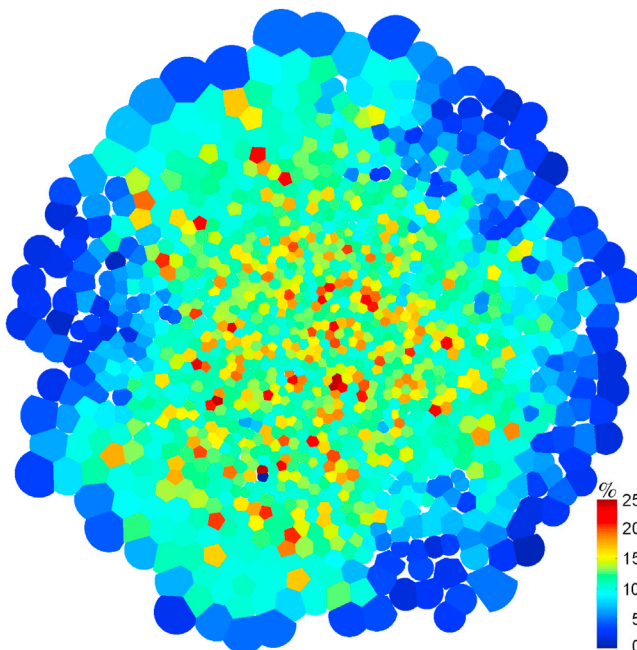


FIGURE 9 Compression of individual cells at the final time. To see this figure in color, go online.

individual cells, which can be measured by atomic force microscopy probe indentation (see, e.g., Sokolov et al. (41)), are much better known. To derive the Young's modulus of an individual cell from such indentation experiments, simple mechanical models are typically used (42). Values for human cervical epithelial cells range from 1 to 20 kPa, depending on the indentation experiment and the mechanical model considered. How these properties for single cells can be related to the mechanical properties of cell colonies remains open. However, another advantage of our approach is that our model can also be parameterized using an experimentally derived direct two-point correlation function to start with (recall the model derivation in Materials and Methods). For example, experimental measurements can provide an approximation of the dynamic structure factor (see, e.g., Angelini et al. (3)). By solving the Ornstein-Zernike integral equation (see, e.g., Caccamo (43)), we can approximate the direct two-point correlation function from the structure factor. We plan to consider this in future work.

SUPPORTING MATERIAL

Supporting Materials and Methods, three figures, and one movie are available at [http://www.biophysj.org/biophysj/supplemental/S0006-3495\(15\)00808-5](http://www.biophysj.org/biophysj/supplemental/S0006-3495(15)00808-5).

AUTHOR CONTRIBUTIONS

A.V. and J.L. conceived the overall design of the research. S.A. derived the mathematical model, discretized and implemented the equations, and conducted the numerical study. S.A., A.V., and J.L. analyzed the results and wrote the article. H.H. contributed in the critical discussions of the model's biological applications and the corresponding parameterization.

ACKNOWLEDGMENTS

The authors thank Zhen Guan for helpful discussions regarding the numerical methods.

S.A., H.H., and A.V. acknowledge support from the German Science Foundation under SPP 1506 A11705/1, SPP 1296 Vo899/7 and EXC CfAED. S.A., H.H., A.V., and J.L. thank the European Commission for support under FP7-PEOPLE-2009-IRSES PHASEFIELD. J.L. is grateful for support from the National Science Foundation Division of Mathematical Sciences and from the National Institutes of Health through grant P50GM76516 for the Center of Excellence in Systems Biology at the University of California, Irvine, and grant P30CA062203 for the Chao Family Comprehensive Cancer Center at University of California, Irvine. Simulations were carried out at Das Zentrum für Informationsdienste und Hochleistungsrechnen at Technische Universität Dresden and the Jülich Supercomputing Center at Forschungszentrum Jülich and at University of California, Irvine. S.A. is also grateful for the hospitality of the Department of Mathematics at the University of California, Irvine, where some of this research was conducted.

REFERENCES

1. Vincent, J.-P., A. G. Fletcher, and L. A. Baena-Lopez. 2013. Mechanisms and mechanics of cell competition in epithelia. *Nat. Rev. Mol. Cell Biol.* 14:581–591.
2. Puliafito, A., L. Hufnagel, ..., B. I. Shraiman. 2012. Collective and single cell behavior in epithelial contact inhibition. *Proc. Natl. Acad. Sci. USA.* 109:739–744.
3. Angelini, T. E., E. Hannezo, ..., D. A. Weitz. 2011. Glass-like dynamics of collective cell migration. *Proc. Natl. Acad. Sci. USA.* 108:4714–4719.
4. Shraiman, B. I. 2005. Mechanical feedback as a possible regulator of tissue growth. *Proc. Natl. Acad. Sci. USA.* 102:3318–3323.
5. Scianna, M., and L. Preziosi. 2012. Multiscale developments of the cellular Potts model. *Multiscal. Model. Simul.* 10:342–382.
6. Farhadifar, R., J.-C. Röper, ..., F. Jülicher. 2007. The influence of cell mechanics, cell-cell interactions, and proliferation on epithelial packing. *Curr. Biol.* 17:2095–2104.
7. Landsberg, K. P., R. Farhadifar, ..., C. Dahmann. 2009. Increased cell bond tension governs cell sorting at the *Drosophila* anteroposterior compartment boundary. *Curr. Biol.* 19:1950–1955.
8. Wartlick, O., P. Mumcu, ..., M. González-Gaitán. 2011. Dynamics of Dpp signaling and proliferation control. *Science.* 331:1154–1159.
9. Vogel, V., and M. Sheetz. 2006. Local force and geometry sensing regulate cell functions. *Nat. Rev. Mol. Cell Biol.* 7:265–275.
10. Rauzi, M., P.-F. Lenne, and T. Lecuit. 2010. Planar polarized actomyosin contractile flows control epithelial junction remodelling. *Nature.* 468:1110–1114.
11. Hannezo, E., J. Prost, and J.-F. Joanny. 2014. Theory of epithelial sheet morphology in three dimensions. *Proc. Natl. Acad. Sci. USA.* 111:27–32.
12. Okuda, S., Y. Inoue, ..., T. Adachi. 2013. Modeling cell proliferation for simulating three-dimensional tissue morphogenesis based on a reversible network reconnection framework. *Biomech. Model. Mechanobiol.* 12:987–996. <http://dx.doi.org/10.1007/s10237-012-0458-8>.
13. Okuda, S., Y. Inoue, ..., T. Adachi. 2015. Coupling intercellular molecular signalling with multicellular deformation for simulating three-dimensional tissue morphogenesis. *Interface Focus.* 5:20140095.
14. Sepúlveda, N., L. Petitjean, ..., V. Hakim. 2013. Collective cell motion in an epithelial sheet can be quantitatively described by a stochastic interacting particle model. *PLOS Comput. Biol.* 9:e1002944.
15. Macklin, P., M. E. Edgerton, ..., V. Cristini. 2012. Patient-calibrated agent-based modelling of ductal carcinoma in situ (DCIS): from microscopic measurements to macroscopic predictions of clinical progression. *J. Theor. Biol.* 301:122–140.
16. Schaller, G., and M. Meyer-Hermann. 2005. Multicellular tumor spheroid in an off-lattice Voronoi-Delaunay cell model. *Phys. Rev. E Stat. Nonlin. Soft Matter Phys.* 71:051910.
17. Chauviere, A., H. Hatzikirou, ..., V. Cristini. 2012. Dynamic density functional theory of solid tumor growth: preliminary models. *AIP Adv.* 2:11210.
18. Marconi, U. M. B., and P. Tarazona. 1999. Dynamical density functional theory of fluids. *J. Chem. Phys.* 110:8032–8044.
19. Elder, K. R., N. Provatas, ..., M. Grant. 2007. Phase-field crystal modeling and classical density functional theory of freezing. *Phys. Rev. B.* 75:064107.
20. van Teeffelen, S., R. Backofen, ..., H. Löwen. 2009. Derivation of the phase-field-crystal model for colloidal solidification. *Phys. Rev. E Stat. Nonlin. Soft Matter Phys.* 79:051404.
21. Elder, K. R., M. Katakowski, ..., M. Grant. 2002. Modeling elasticity in crystal growth. *Phys. Rev. Lett.* 88:245701.
22. Elder, K. R., and M. Grant. 2004. Modeling elastic and plastic deformations in nonequilibrium processing using phase field crystals. *Phys. Rev. E Stat. Nonlin. Soft Matter Phys.* 70:051605.
23. Provatas, N., J. A. Dantzig, ..., K. R. Elder. 2007. Using the phase-field crystal method in the multiscale modeling of microstructure evolution. *JOM.* 59:83–90.
24. Provatas, N., and K. Elder. 2010. Phase-Field Methods in Materials Science and Engineering. Wiley, New York.

25. Emmerich, H., H. Löwen, ..., L. Gránásy. 2012. Phase-field-crystal models for condensed matter dynamics on atomic length and diffusive time scales: an overview. *Adv. Phys.* 61:665–743.
26. Li, J. F., and J. Lowengrub. 2014. The effects of cell compressibility, motility and contact inhibition on the growth of tumor cell clusters using the Cellular Potts Model. *J. Theor. Biol.* 343:79–91.
27. Patel, A. B., W. T. Gibson, ..., R. Nagpal. 2009. Modeling and inferring cleavage patterns in proliferating epithelia. *PLOS Comput. Biol.* 5:e1000412.
28. Bentley, J. L. 1975. Multidimensional binary search trees used for associative searching. *Commun. ACM.* 18:509–517.
29. Alarcón, T., H. M. Byrne, and P. K. Maini. 2005. A multiple scale model for tumor growth. *Multiscale Model. Simul.* 3:440–475.
30. Aegerter-Wilmsen, T., A. C. Smith, ..., K. Basler. 2010. Exploring the effects of mechanical feedback on epithelial topology. *Development.* 137:499–506.
31. Staple, D. B., R. Farhadifar, ..., F. Jülicher. 2010. Mechanics and remodelling of cell packings in epithelia. *Eur Phys J E Soft Matter.* 33:117–127.
32. Axelrod, J. D. 2006. Cell shape in proliferating epithelia: a multifaceted problem. *Cell.* 126:643–645.
33. Nagpal, R., A. Patel, and M. C. Gibson. 2008. Epithelial topology. *Bio-Essays.* 30:260–266.
34. Gibson, W. T., J. H. Veldhuis, ..., M. C. Gibson. 2011. Control of the mitotic cleavage plane by local epithelial topology. *Cell.* 144:427–438.
35. Backofen, R., A. Voigt, and T. Witkowski. 2010. Particles on curved surfaces: a dynamic approach by a phase-field-crystal model. *Phys. Rev. E Stat. Nonlin. Soft Matter Phys.* 81:025701.
36. Backofen, R., M. Gräf, ..., T. Witkowski. 2011. A continuous approach to discrete ordering on S^2 . *Multiscale Model. Simul.* 9:314–334.
37. Schmid, V., and A. Voigt. 2014. Crystalline order and topological charges on capillary bridges. *Soft Matter.* 10:4694–4699.
38. Aland, S., A. Rätz, ..., A. Voigt. 2012. Buckling instability of viral capsids - a continuum approach. *SIAM MMS.* 10:82–110.
39. Lewis, F. 1928. The correlation between cell division and the shapes and sizes of prismatic cells in the epidermis of cucumis. *Anat. Rec.* 38:341–376.
40. Aland, S., J. Lowengrub, and A. Voigt. 2011. A continuum model of colloid-stabilized interfaces. *Phys. Fluids.* 23:062103.
41. Sokolov, I., M. E. Dokukin, and N. V. Guz. 2013. Method for quantitative measurements of the elastic modulus of biological cells in AFM indentation experiments. *Methods.* 60:202–213.
42. Guz, N., M. Dokukin, ..., I. Sokolov. 2014. If cell mechanics can be described by elastic modulus: study of different models and probes used in indentation experiments. *Biophys. J.* 107:564–575.
43. Caccamo, C. 1996. Integral equation theory description of phase equilibria in classical fluids. *Phys. Rep.* 274:1–105.